PAPER

Fibronectin-tethered graphene oxide as an artificial matrix for osteogenesis

To cite this article: Ramesh Subbiah *et al* 2014 *Biomed. Mater.* **9** 065003

View the article online for updates and enhancements.

Related content

- 3D cell culture and osteogenic differentiation of human bone marrow stromal cells plated onto jet-sprayed or electrospun micro-fiber scaffolds
Meadhbh Á Brennan, Audrey Renaud, Anne-laure Gamblin et al.

- Development of novel silk fibroin/polyvinyl alcohol/sol-gel bioactive glass composite matrix by modified layer by layer electrospinning method for bone tissue construct generation
B N Singh and K Pramanik

- The promising application of graphene oxide as coating materials in orthopedic implants: preparation, characterization and cell behavior
Changhong Zhao, Xiuzhen Lu, Carl Zanden et al.

Recent citations

- Evaluation of physico-mechanical properties in NHDF and HeLa cell with treatment of graphene quantum dots using atomic force microscopy
Seong-Beom Jeon *et al*

- Non-viral approaches for direct conversion into mesenchymal cell types: Potential application in tissue engineering
Eun-Seo Lee *et al*

- Graphene and graphene-based nanocomposites: biomedical applications and biosafety
Satyanarayan Pattnaik *et al*

Fibronectin-tethered graphene oxide as an artificial matrix for osteogenesis

Ramesh Subbiah[1,2]**, Ping Du**[1,2]**, Se Young Van**[1,2]**, Muhammad Suhaeri**[1,2]**,
Mintai P Hwang**[2]**, Kangwon Lee**[1,2] **and Kwideok Park**[1,2]

[1] Department of Biomedical Engineering, Korea University of Science and Technology (KUST), Daejon,
305–333, Korea
[2] Center for Biomaterials, Korea Institute of Science and Technology (KIST), Seoul, 136–791, Korea

E-mail: kpark@kist.re.kr

Abstract

An artificial matrix (Fn-Tigra), consisting of graphene oxide (GO) and fibronectin (Fn), is
developed on pure titanium (Ti) substrates via an electrodropping technique assisted with a
custom-made coaxial needle. The morphology and topography of the resulting artificial matrix
is orderly aligned and composed of porous microcavities. In addition, Fn is homogenously
distributed and firmly bound onto GO as determined via immunofluorescence and elemental
mapping, respectively. The artificial matrix is moderately hydrophobic ($63.7°$), and exhibits
an average roughness of 546 nm and a Young's modulus (E) of approximately 4.8 GPa. The
biocompatibility, cellular behavior, and osteogenic potential of preosteoblasts on Fn-Tigra
are compared to those of cells cultured on Ti and Ti-GO (Tigra). Cell proliferation and
viability are significantly higher on Fn-Tigra and Tigra than that of cells grown on Ti. Focal
adhesion molecule (vinculin) expression is highly activated at the central and peripheral area
of preosteoblasts when cultured on Fn-Tigra. Furthermore, we demonstrate enhanced *in vitro*
osteogenic differentiation of preosteoblasts cultured on Fn-Tigra over those cultured on bare
Ti, as determined via Alizarin red and von Kossa staining, and the analysis of osteocalcin,
type I collagen, alkaline phosphatase activity, and calcium contents. Finally, we investigate
the biophysical and biomechanical properties of the cells using AFM. While the height and
roughness of preosteoblasts increased with time, cell surface area decreased during *in vitro*
osteogenesis over 2 weeks. In addition, the E of cells cultured on Tigra and Fn-Tigra increase
in a statistically significant and time-dependent manner by 30%, while those cultured on bare
Ti retain a relatively consistent E. In summary, we engineer a biocompatible artificial matrix
(Fn-Tigra) capable of osteogenic induction and consequently demonstrate its potential in bone
tissue engineering applications.

Keywords: graphene oxide, fibronectin, titanium, electrodropping system, osteogenic
differentiation, atomic force microscopy

(Some figures may appear in colour only in the online journal)

1. Introduction

Extracellular matrix (ECM) is a well-organized network of a variety of proteins, proteoglycans, and other components. The hierarchical ECM structure provides a three-dimensional (3D) microenvironment, in which various micro- and nano-structures are fully established. Increasing studies have suggested a great influence of these ECM structural features on cellular behavior. Not surprisingly, extensive research is underway with regards to the elucidation of the ECM microenvironment and the fabrication of engineered biomimetic two-dimensional (2D) and 3D constructs for tissue engineering and regenerative medicine [1–4]. However, despite the numerous studies of ECM, it is still extremely challenging to mimic ECM environment together with chemical, physical and mechanical cues

using micro- and nanotechnology [5]. Nonetheless, nano-patterns and nano-featured biomaterials are of great interest in that they confer the ability to engineer a biomimetic artificial microenvironment [6–8]. For example, electrospun polymeric nanofibers [9], carbon nanotubes (CNTs [10]), inorganic nanomaterials [11], and graphene [12–14] have been investigated for the study of stem cell lineage specification, growth factor delivery, and other biomedical applications. Among them, graphene oxide (GO), an oxidized derivative of graphene, is an attractive candidate in constructing the cellular microenvironment for bone tissue engineering applications, due to its tunable physicochemical properties, bone-like stiffness, low friction coefficient against bone, flexible design, and biomolecule storage capacity [12–14]. However deposition of GO in a nanotopographical pattern is very difficult and it is dependent on the substrate characteristics where GO interacts.

In this study, we use an electrodropping system assisted with a coaxial needle [15] to generate orderly aligned microcavity structures combined with nanotopographic features conferred by strongly adherent GO sheets on titanium (Ti) disks (hereafter mentioned as 'Tigra'). In addition, Fn is used to surface functionalize Tigra as a means to generate cell-binding motifs. Morphology and structural arrangements of Fn-anchored Tigra (Fn-Tigra) are further characterized and compared with Ti and Tigra. Early studies have documented the vital functions of ECM biomolecules, such as fibronectin (Fn) [16–18], collagen [19] and laminin [20] in creating nanotopographical substrate modifications and in manipulating cellular behaviors. Dolatshahi-Pirouz *et al* revealed Fn adsorption on various nanostructured surface positively influenced the stem cell behavior and interaction [17]. Keselowsky *et al* reported the control of cell adhesion by modulating Fn conformation [21]. We hypothesize that Fn-Tigra can act as an artificial matrix microenvironment to enhance the adhesion of preosteoblasts and their osteogenic differentiation. Live and dead cell assay, CCK-8 assay, Alizarin red and von Kossa staining, analysis of osteogenic marker (osteocalcin and type I collagen) expression, alkaline phosphatase (ALP) activity, and calcium content demonstrate the biocompatibility of Fn-Tigra and its enhanced osteogenic potential over that conferred by Ti or Tigra.

Additionally, we explore some biophysical and biomechanical characteristics of preosteoblasts during osteogenesis via atomic force microscopy (AFM). While numerous studies have utilized AFM for the biomechanical analysis of cells [22, 23], breast cancer [24], internal lining membrane [25], osteoarthritis [26], and stem cell differentiation potential [27], biomechanical changes experienced by differentiating cells on a temporal basis are less well understood. Our hypothesis is that differentiating cells experience both phenotype alterations (cell) and ECM concentrations (microenvironment). These changes may be monitored using biophysical and biomechanical factors. Along with some biophysical parameters (roughness, spreading area, and cell height), we selected cell stiffness (Young's modulus; E) as a biomechanical marker. In addition to the conventional biological and biochemical tools, the implications of E as an osteogenic biomarker may provide another insight in understanding the pathway of cellular differentiation.

2. Experimental section

2.1. Preparation of GO and Ti disks

GO was synthesized using a modified Hummers protocol as described in previous reports [28, 29]. Briefly, graphite flakes were mixed with a solution of concentrated sulfuric acid (H_2SO_4), sodium nitrate ($NaNO_3$), and potassium permanganate ($KMnO_4$). The mixture was then heated to 50 °C, stirred for 12 h, and cooled to room temperature (RT). The reaction product was poured onto ice in 30% hydrogen peroxide (H_2O_2), sifted using a metal sieve (300 μm), and filtered through a polyester fiber (Carpenter Co.). After centrifugation at 4000 rpm for 4 h, the supernatant was decanted away, and the remaining precipitate was washed with 200 ml of water several times, 200 ml of 30% hydrochloric acid (HCl) and 200 ml of ethanol two times. Upon washing, 200 ml of ether was added to the precipitate. The resulting suspension was filtered through a PTFE membrane with a 0.45 μm pore size, dialyzed against distilled water (DW) until a pH of at least 5 was obtained, and vacuum-dried overnight. Commercially pure Ti plates (Nilaco Corporation, Japan) were cut into disks (1 mm thick and 15 mm in diameter), polished, and washed with acetone, methanol, ethanol, and isopropyl alcohol, three times each. The Ti specimens were autoclaved, stored in a vacuum oven at 50 °C, and used for the electrodrop-casting of GO without further processing. All reagents and materials for synthesis were purchased from Sigma-Aldrich (USA), Alfa Aesar (UK), Daejung Chemicals & Metals Co. Ltd, (South Korea), and Daihan Scientific (South Korea).

2.2. Fabrication of tigra and functionalization with Fn

GO was synthesized and used in the fabrication of Fn-Tigra as described in figure 1(*a*). GO solution in dimethylfuran (DMF) was deposited on a Ti substrate using the electrodropping system [15], in which 18G and 26G stainless steel nozzles were employed as the outer and inner nozzle, respectively. A dual syringe pump system was used to control the flow rate of each solution—0.05 ml min^{-1} and 0.1 ml min^{-1} for the inner and outer syringes, respectively—while a 15–18 kV dc voltage was applied to the needle to initiate electrodropping of GO solution onto Ti disks, which are placed onto a collecting plate. The X–Y axis movement was kept constant and the distance between the needle and collector was 15 cm. The resultant Tigra was calcined at 55 °C before further use. For functionalization of Tigra using Fn, samples were placed in 6-well plates, incubated with Fn solution (50 μg ml^{-1}) at 37 °C for 2 h, washed with PBS, and air-dried under a fume hood.

2.3. Surface characterization

The surface morphology and properties of Fn-functionalized Tigra were characterized via Scanning electron microscope (SEM) at an accelerating voltage of 20 kV and via EDS at 200 kV (SEM-EDS; Inspect F50, FEI Company, Hillsboro, OR, USA). Surface topography was also evaluated using an atomic force microscope (Bio-AFM; NanoWizard II, JPK Instruments, Berlin, Germany) equipped with an inverted
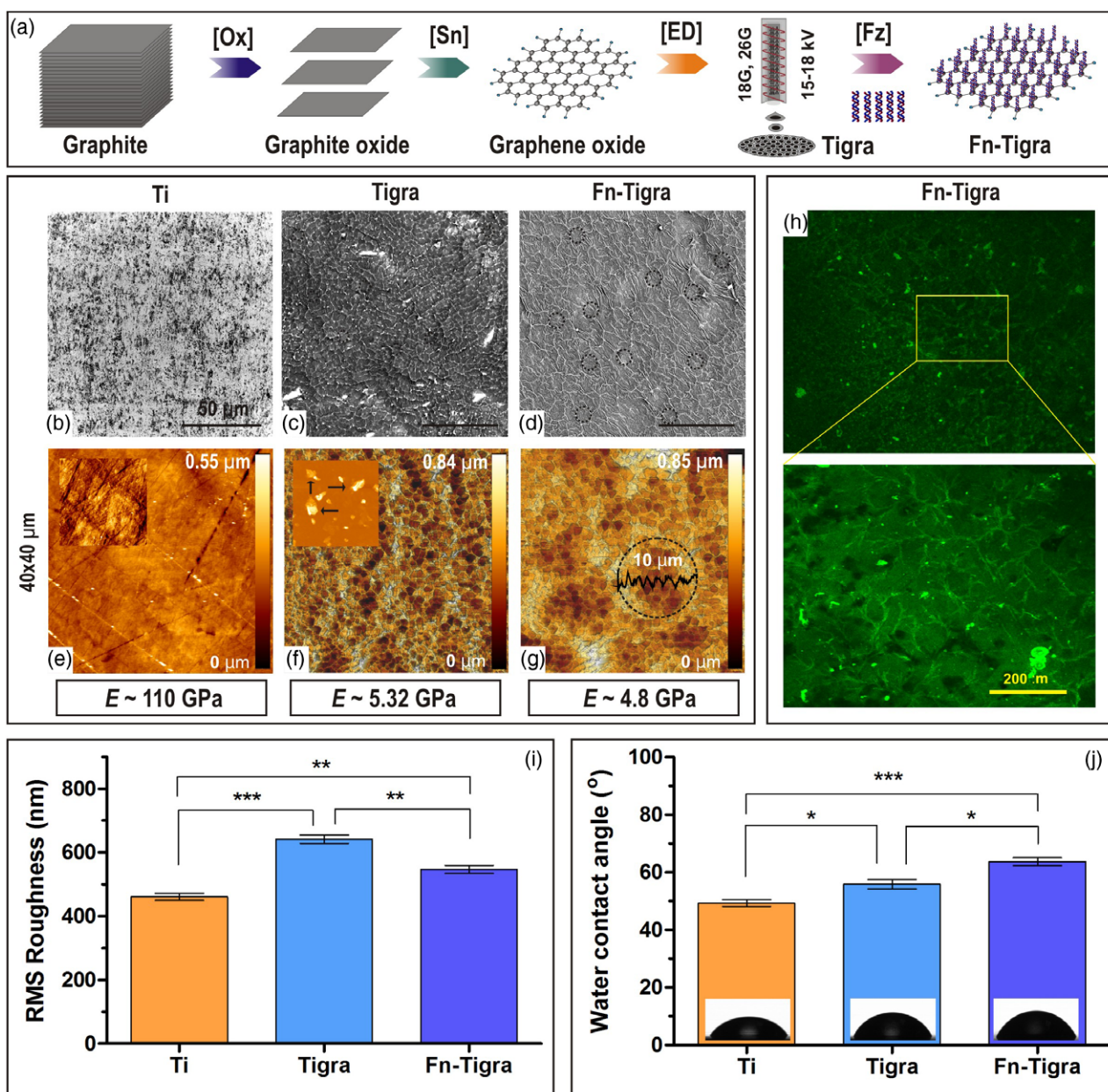
Figure 1. Schematic illustration of Fn-Tigra preparation and surface characterization of Ti, Tigra and Fn-Tigra. (*a*) Schematic describes the synthesis route for GO and fabrication of Fn-Tigra, where [Ox], [Sn], [ED] and [Fz] denote oxidation, sonication, electrodropping, and Fn functionalization, respectively. (*b*), (*c*), (*d*) SEM images and (*e*), (*f*), (*g*) AFM images of Ti, Tigra and Fn-Tigra exhibit different surface textures and topography. Inset (f–arrows) shows individual GO flakes and micro-porous rich hollow structures (g–circle). The average thickness of matrix on Ti substrate is depicted as a line profile inside the marked circle (*g*). The average stiffness (*E*) of Ti, Tigra and Fn-Tigra substrates is shown. Bioactive Fn on Fn-Tigra is confirmed by IFS (*h*), and upon magnification, Fn moieties are homogenously distributed over the periphery of cavities. Quantitative results including surface roughness (*i*) and water contact angle (*j*) are shown. Statistically significant differences among Ti, Tigra and Fn-Tigra are marked as * ($p < 0.05$), ** ($p < 0.01$) or *** ($p < 0.001$).

optical microscope (Nikon). The root mean square (rms) roughness (R_q) was subsequently determined using analytical software (JPK Data Processing). In addition, x-ray diffraction was analyzed via XRD (SOL-XE, Bruker x-ray diffractometer, Karlsruhe, Germany) using a Cu Kα line (λ- 1.54056Å) at a setting of 30 kV and 300 mA; the 2θ angle is varied from 5° to 90° at a rate of 2° min^{-1}. Furthermore, the Raman spectrum of the GO film was measured (MonoRa500i, Dongwoo Optron Co., Ltd, South Korea). Finally, the surface wettability was investigated via contact angle measurements (GBX, France).

2.4. Immunofluorescence staining of functionalized Fn

Fn-Tigra was gently washed with phosphate-buffered saline (PBS) and incubated with primary antibody of mouse anti-fibronectin in 1% BSA (1:50) at 4 °C overnight. Upon thorough washing, the samples were then incubated with Alexa Fluor 488-conjugated goat anti-mouse IgG in 1% BSA (1:200) at RT for 1 h. The distribution of functionalized Fn was observed using a confocal laser scanning microscope (Olympus FluoView FV1000, Tokyo, Japan).

2.5. Cell morphology, viability and proliferation

Preosteoblasts (2×10^4 cm^{-2}, MC3T3-E4, ATCC, Manassas, VA) were seeded onto the substrates (Ti, Tigra, and Fn-Tigra) and cultured in minimum essential medium alpha (α-MEM) supplemented with 10% fetal bovine serum (FBS) and 1% penicillin/streptomycin (P/S). To test for cell viability, the medium was removed at 24 h and replaced with a mixture of PBS (1 ml), 2 μM calcein AM, and 4 μM ethidium bromide, and incubated at RT for 15 min. After the samples were washed several times, the live and dead cells were visualized via fluorescence microscopy (CKX41-F32FL; Olympus). The cell proliferation rate was measured on day 1 and 3 according to the manufacturer's instructions (CCK-8; Dojindo, Japan), in which 10% CCK-8 solution was added to samples, incubated at 37 °C for 2 h, and measured for absorbance at 450 nm using a Multiscan microplate reader (Thermo Scientific, Rockford, IL). Finally, cell morphology on each substrate was examined via SEM (Phenom G2 pro desktop, Eindhoven, Netherlands); on day 3, cells were fixed, serially dehydrated in graded ethanol solution (50–100%), completely dried, and sputter-coated with platinum.

2.6. Focal adhesion assay

Fluorescence staining of the cytoskeleton (F-actin), a focal adhesion (FA) molecule (vinculin), and the cell nucleus was performed in order to examine how the FA assembly pattern changes for cells cultured on different substrates. After rinsing with PBS buffer twice, cells were permeabilized with 0.1% Triton X-100. After another washing step, the cells were then incubated with 1% BSA blocking solution at RT for 15 min, and subsequently washed with PBS buffer twice. Cells were then incubated with mouse monoclonal anti-vinculin (0.67 μg ml^{-1}) at 37 °C for 1 h, washed with PBS three times, and incubated with 10 μg ml^{-1} of fluorescein isothiocyanate (FITC)-conjugated goat anti-mouse IgG (Chemicon International, Temecula, CA) and 37.5 ng ml^{-1} tetramethyl rhodamine isothiocyanate (TRITC)-conjugated phalloidin at RT for 1 h. Cells were washed three times, incubated with 4,6-diamidino-2-phenylindole (DAPI) solution for 5 min, and rinsed with PBS several times. Fluorescence-stained cells were kept in PBS at 4 °C before analysis via confocal microscopy (Olympus FluoView FV1000, Tokyo, Japan). The FA pattern of each cell was quantified with respect to the number of FA spots, the FA area, and the diameter of single FA spots using image processing software (Image J). A pre-processing step, in which the local contrast of each image was enhanced using the color display option, was implemented to aid in the identification of vinculin expression. The mean spot size and circularity was set to 1 μm^2 while the background was minimized using the intensity modulator. Three independent samples were examined for each group and fifteen separate regions were imaged for each sample using confocal microscope.

2.7. Induction of osteogenic differentiation in vitro and analysis

Preosteoblasts were seeded in 6 well plates at 2×10^4 cells cm^{-2} and cultured in osteogenic medium for 2 weeks under standard cell culture conditions (humidified atmosphere with 5% CO$_2$). Osteogenic media consists of α-MEM supplemented with 10% FBS, 1% P/S, 10 mM β-glycerophosphate, 0.1 μM dexamethasone, 50 μg ml^{-1} L-ascorbic-2-phosphate, and 50 ng ml^{-1} bone morphogenetic protein 2 (BMP-2) (Korea Bone Bank, Seoul, Korea [30]). The medium was changed every 2 d and analyzed via various assays on days 7 and 14.

2.8. Immunofluorescence staining of osteogenic marker proteins

Osteocalcin (OC) and type I collagen (Col I) expression was measured on days 7 and 14. Differentiated cells were fixed, gently washed with PBS, treated with peroxo-block solution for 1 min, and washed with PBS several times. The cells were then permeabilized using 0.1% Triton X-100 for 5 min, blocked with 3% BSA for 2 h, and incubated with either rabbit anti-osteocalcin antibody or goat anti-type I collagen antibody in 1% BSA (1 : 50) overnight at 4 °C. The samples were then reacted with Alexa Fluor 488-conjugated goat anti-mouse IgG or Alexa Fluor 594-conjugated donkey anti-goat IgG in 1% BSA (1 : 200) for 1 h at RT. Immunostained specimens were further subjected to DAPI staining for nucleic staining of cells. Fluorescent signals of the target proteins were detected via confocal microscopy (Olympus).

2.9. Alizarin red and von Kossa staining

Day 7 and 14 samples were fixed in 4% ρ-formaldehyde for more than 30 min and washed with DW three times. For Alizarin red staining of calcium deposition, samples were stained with a 2% Alizarin red solution (pH 4.2) for 10 min and washed with DW. For von Kossa staining of phosphate (mineralized matrices), samples were immersed in 5% silver nitrate (AgNO$_3$) solution under ultraviolet light for 1 h, treated with sodium carbonate/formaldehyde for 1 min, reacted with 5% sodium thiosulfate (Na$_2$S$_2$O$_3$) solution for 5 min, rinsed with DW, serially dehydrated in graded ethanol solution (50%, 75%, 100%), and air-dried. Red and black or brownish-black colored spots were observed via portable SEM. Positively stained areas were quantified via image processing software (Image J, NIH).

2.10. Measurement of ALP activity and calcium content

ALP activity was evaluated using an ALP kit (LabAssay, Wako Pure Chemicals Industries, Japan) according to the manufacturer's instructions. Day 7 and 14 samples were lysed using a 0.5% Triton X-100 solution, collected via substrate surface scraping, and vortexed for 30 min. 5 μl of each sample was mixed with 200 μl of working reagent, incubated for 3 min at RT, and measured for absorbance at 405 nm using a micro plate reader (Thermo Scientific). The amount of calcium deposition was investigated using a QuantiChrom Calcium Assay Kit (DICA-500, BioAssay systems, USA) according to the manufacturer's instructions. ALP activity and calcium content was normalized using total protein concentration, which

was determined using a bicinchoninic acid (BCA) assay kit (Pierce).

2.11. Biophysical and biomechanical analysis

Changes to biophysical (cell height, spreading area, and roughness) and biomechanical characteristics (E) of differentiating preosteoblasts were monitored at multiple time points (days 1, 3, 7 and 14) via Bio-AFM (JPK Instruments). A HYDRA2R-50NG probe was used in contact mode and the scan size was adjusted to $100 \times 100\,\mu m^2$ to accommodate for typical surface features while maintaining a high resolution. A CONT-S sphere probe (400 nm radius; Nanoworld Services GmbH, Erlangen, Germany) with a $0.4\,N\,m^{-1}$ force constant was employed for E measurements; indentation measurements were carried out immediately after scanning the area of interest using the same probe. The ramp size and loading speed were set to $1\,\mu m$ and $1\,\mu m\,s^{-1}$, respectively. A series of indentation forces (0.5–10 nN) were tested to calibrate the indentation depth in the range of 50–500 nm in order to prevent cell surface defects and Hertz model limitation. Tip-sample separation curves and the E was determined via Hertz's contact model using JPK data processing software (JPK instruments), in which the Poisson's ratio was set to 0.5. The average E for each sample was calculated from 10–20% of the indentation depth out of the total measured cell height.

2.12. Statistical analysis

All data was obtained from three samples ($n = 3$), and repeated for three independent experiments. The data are presented as mean ± SD. A one-way ANOVA was performed to assess a statistical significance and the difference is considered statistically significant if p is less than 0.05.

3. Results and discussion

3.1. Characterization of artificial matrix

Artificial matrices conferred with an instructive microenvironment offer great advantages to the study of tissue engineering, regenerative medicine, and bionanotechnology [3, 4]. The employment of self-assembled graphene or GO is an interdisciplinary field with latent applications in various biomedical sciences [12–14]. However, there are still not many cases reported. The present work describes the preparation of Tigra, a GO-based artificial matrix, and its bio-functionalization with Fn. Ti was selected as a control group in determining the potential of Tigra and Fn-Tigra for inducing osteogenesis. The fabrication process of Fn-Tigra is illustrated in figure 1(*a*). Briefly, the modified Hummer's method was applied for the synthesis of GO [13, 28, 29] and Tigra was prepared via an optimized electrodropping system equipped with a precisely controlled coaxial needle [15]. Compared to the Ti surface (figure 1(*b*)), an artificial matrix with micro-cavities and orderly aligned hollow spaces on Ti substrates was fabricated using the system (figures 1(*c*) and (*d*)), in which control

over the flow rate of GO solution led to the self-assembly of GO in a spatially oriented manner. SEM images indicate the presence of relatively uniform porous and cavity-like structures (marked as dotted circles) with defined boundaries (figure 1(*d*)). Electrodropping of GO solution at high electric field forms strong deposition of graphene flakes on titanium. Titanium atoms interact with the graphene molecules, wherein metal atoms act as electron donors, and graphene oxide act as acceptors. This bonding prevents delamination of Graphene oxide layer from titanium surface. GO sheets in the artificial matrix were detected via AFM (figure 1(*f*), inset) and the average diameter and depth of a porous hollow cavity was ~10 μm and ~800 nm, respectively (figure 1(*g*)), while the thickness of the GO matrix on the Ti substrate was found to be ~2 μm. In particular, the sub-distribution of an interconnected microporous structure within the marked circle in figure 1(*g*) is notable. Given that the size, shape, and height of these porous hollow spaces can be manipulated by altering the inner needle flow rate of the GO solution, our results corroborate the capacity of the electrodropping technique for the generation of unique surface textures, including cavities and orderly aligned porous hollow spaces of μm to nm resolution. Additional AFM images ($40 \times 40\,\mu m^2$ scale) depict the relatively smooth surface of polished Ti substrates (R_q ~ 461.1 nm), as compared to that of Tigra (R_q ~ 641.4 nm) (figures 1(*e*)–(*g*) and (*i*)). Tigra was subsequently bio-functionalized by Fn that was surface-adsorbed more in the periphery of micro-cavities in Tigra. Tigra extends the capacity to act as a substrate for the attachment of FN specifically due to its hydrophilic and rough surface. Fn is immobilized via electrostatic interactions and nontrivial adsorption effects with the oxygenated groups of GO, which is in accordance with the early studies [18, 31, 32]. The Fn on the Fn-Tigra is confirmed by immunofluorescence staining (IFS) (figure 1(*h*)). In addition, nanoindentation measurements revealed that the E of Tigra (~5.3 GPa) decreased to ~4.8 GPa after the surface functionalization of Fn. Furthermore, water contact angle measurements indicate a relatively hydrophilic surface for Tigra (figure 1(*j*)). That of Fn-Tigra increases while the roughness decreases (~546 nm) when compared to Tigra (~641 nm). The observed changes are likely due to enhanced Fn adsorption on the surface of Tigra.

Meanwhile XRD patterns for Tigra and Fn-Tigra illustrate a strong and sharp (0 0 2) diffraction peak at $2\theta = $ ~12°, different from that observed for Ti (figure 2(*a*), inset [33]). In addition, Raman spectroscopy of Tigra and Fn-Tigra indicates the presence of three distinguished peaks at ~1347 cm^{-1}, ~1584 cm^{-1} and ~2675 cm^{-1}, representing the D band, G band and 2D band of GO, respectively (figure 2(*b*) [33]). The distinct peaks of Fn were undetected due to overlap with peaks of GO. Finally, the surface functionalization of Tigra with Fn is confirmed using SEM–energy dispersive x-ray spectroscopy (EDS), elemental mapping and IFS imaging of Fn. Specific elements of Fn-Tigra—Ti (Ti-K), C (C-K), O (O-K) and N (N-K)—were identified (figure 2(*c*)); EDS results indicate the lack of a nitrogen peak for Tigra and a distinct N (N-K) peak for Fn-Tigra (figure 2(*c*)). The compositional ratio between C and N was found to be 1.7:1 and numerous dots were spotted
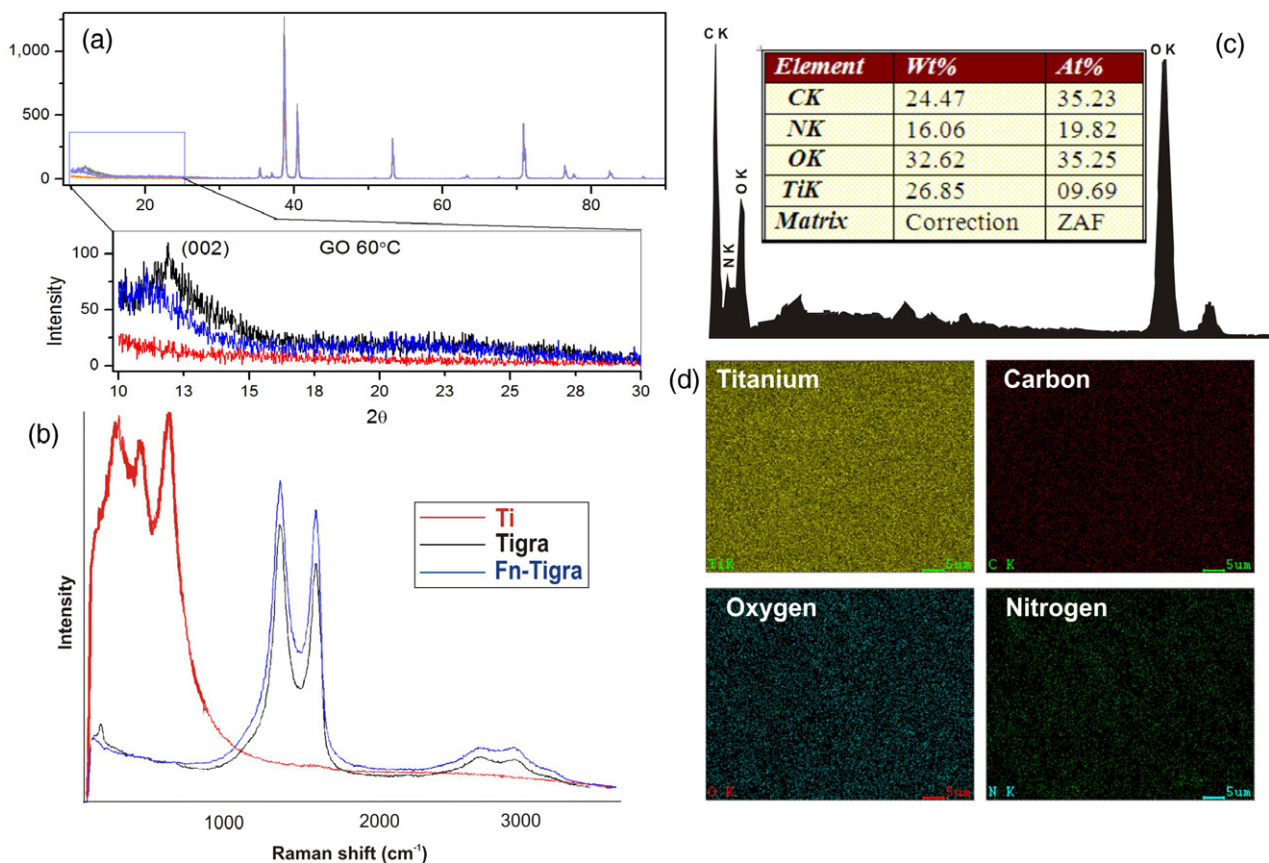
Figure 2. (*a*) XRD, (*b*) Raman and (*c*) EDS spectra of each substrate. (*d*) Elemental mapping of Fn-Tigra shows the presence of nitrogen, oxygen, carbon and Ti. Fn-Tigra exhibits a homogeneous distribution of Fn as confirmed by nitrogen mapping.

uniformly on the Fn-Tigra (figures 2(*c*) and (*d*)). IFS images of Fn further support the adsorption of Fn on Tigra (figure 1(*h*)), and exhibit a strong positive signal at the peripheral region of each island formed on Tigra. Despite some studies regarding protein immobilization on nanomaterial substrates [34], the effects of GO tethered with Fn on cellular adhesion and differentiation remain mostly unknown.

3.2. Preosteoblasts morphology, viability and proliferation

No significant difference in cell viability is observed between cells grown on Tigra and Fn-Tigra for the first 24 h, while those grown on Ti exhibit some cell death (figures 3(*a*)–(*c*) and (*g*)). Similarly, cell proliferation was relatively poor for the Ti group but highest for the Fn-Tigra group as determined via a CCK-8 assay at different time points (days 1 and 3; figure 3(*h*)). Cells grown on Tigra show some improvement with regards to cell adhesion and proliferation when compared to those on Ti. The filopodia connections around preosteoblasts cultured on Tigra and Fn-Tigra were developed, while those of cells cultured on Ti exhibited a different morphology (figure 3(*d*)–(*f*)). Extensive filopodia formation, indicative of enhanced cell migration and cell–cell interactions, was noticed particularly on the Fn-Tigra, due mainly to the RGD binding moieties of Fn which is responsible for cell attachment, organization of the cytoskeleton, and proliferation [31]. Meanwhile, the stability of Fn-Tigra before and after preosteoblast attachment

was investigated via Fourier transform infrared spectroscopy (FTIR) (data not shown); the presence of dominant GO peaks at ~3270, 2960 and 1700–1600 cm^{-1} indicates that the artificial matrix remains secure.

3.3. FA assay

Cell surface integrins transmit diverse extracellular signals via FA molecules, which are connected to actin cytoskeleton. To investigate FA assembly on different substrates, preosteoblasts cultured on Ti, Tigra and Fn-Tigra were analyzed for expression of a FA molecule (vinculin) via IFS at 24 h (figure 4). All groups exhibited a different FA pattern (figures 4(*a*)–(*f*)). In particular, vinculin expression of cells on Ti (figures 4(*a*) and (*d*)) was highly localized around the nuclear region, while that of cells on Tigra and Fn-Tigra (figures 4(*b*), (*c*), (*e*) and (*f*)) was spread over a larger area. Quantification of the number of FA molecules, FA area per cell, and single FA diameter demonstrates that Fn-Tigra provides a beneficial surface nanotopography for cell adhesion and resultant FA formation (figures 4(*g*)–(*i*)); the difference of these quantitative measures between Fn-Tigra and Ti groups was statistically significant. One report exhibits that surface nanotopography can modulate FA assembly, cells spreading, actin CSK organization, and ultimately stem cell differentiation through mechanotransduction involving FA kinase [35].
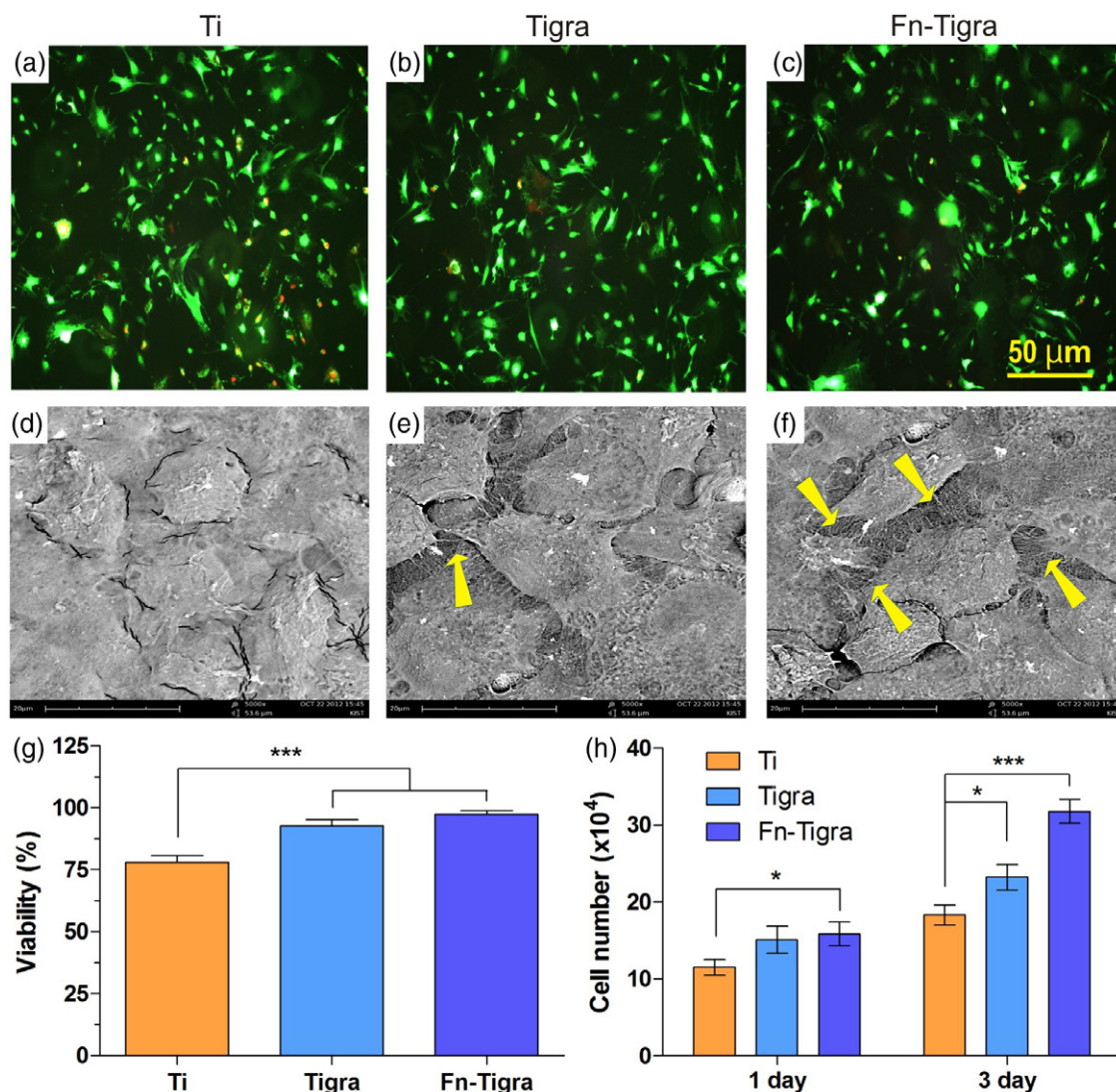
Figure 3. Determination of cell viability, cell morphology, and cell proliferation. (*a*), (*b*), (*c*) Live and dead cell assay (Calcein AM/green/ live cells; Ethidium homodimer/red/dead cells) after 24 h culture on Ti, Tigra and Fn-Tigra, respectively. (*d*), (*e*), (*f*) SEM images of cell adhesion on different substrates. Active filopodia development and cell–cell connection are denoted by yellow arrows. (*g*) Quantification of cell viability at day 1 using live and dead cell assay images. (*h*) Cell proliferation rate was determined for days 1 and 3 using a CCK-8 assay. Statistically significant differences among Ti, Tigra and Fn-Tigra are marked as * ($p < 0.05$) or *** ($p < 0.001$).

3.4. Osteogenic differentiation of preosteoblasts

The feasibility of GO-based artificial matrices (Tigra and Fn-Tigra) as an osteogenic platform was assessed via the *in vitro* culture of preosteoblasts for 2 weeks. Positive signals of osteocalcin (OC/green) and type I collagen (Col I/ red) at days 7 and 14 were much stronger for cells cultured on Fn-Tigra than for those cultured on Ti and Tigra (figures 5(*a*) and (*b*)). Qualitative analysis using Alizarin red staining indicates higher levels of osteogensis for cells cultured on Fn-Tigra than those cultured on Ti (figure 6(*a*)—inset). A similar trend was observed in von Kossa staining (figure 6(*b*)—inset). Furthermore, the intensity levels of Alizarin red and von Kossa stains were also quantitatively analyzed (figures 6(*a*) and (*b*)). Another important osteogenic assays, such as ALP activity (figure 6(*c*)) and calcium content (figure

6(*d*)), were also carried out. The total protein level was higher in the Fn-Tigra group than in Ti and Tigra groups (data not shown); after normalized by total protein content, the ALP activity of cells cultured on Fn-Tigra was 3-fold higher than that of cells cultured on Ti. Likewise, the calcium content of cells cultured on Fn-Tigra was 1.5-fold higher than that of cells cultured on Ti. These data suggest that the artificial matrix (Fn-Tigra) plays a positive role in osteogenic differentiation of preosteoblasts. A major difference between Tigra and Fn-Tigra is the presence of cell-adhesion moieties conferred by Fn. It is generally accepted that Fn-coated surface provides a better microenvironment for cell adhesion and proliferation. The preosteoblasts on Fn-Tigra exhibit not only significantly different morphology but also unique FA assembly when compared to those cultured on Ti and Tigra (figure 4). In particular, cells cultured on Fn-Tigra exhibited active
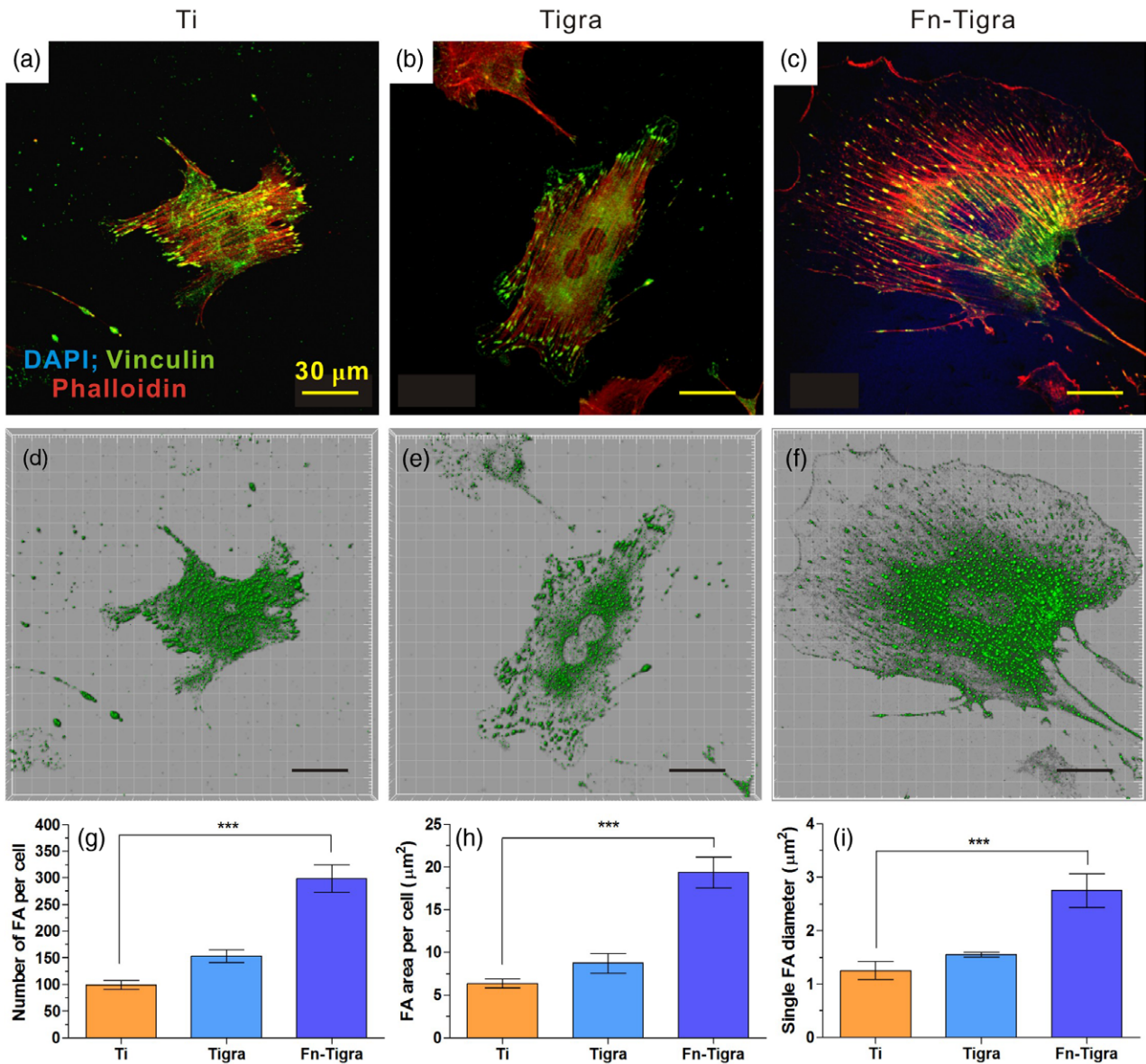
Figure 4. Observation of FA of preosteoblasts cultured for 24 h on (*a*), (*d*) Ti, (*b*), (*e*) Tigra and (*c*), (*f*) Fn-Tigra. Immunofluorescence images of F-actin phalloidin (red), vinculin (green), and DAPI (blue) staining (*a*)–(*c*) and the 3D images for FA distribution and its size (*d*)–(*f*). Quantitative results include the (*g*) number of FA per cell, (*h*) FA area per cell and (*e*) average FA diameter. Statistically significant differences among Ti, Tigra, and Fn-Tigra are marked as *** ($p < 0.001$).

vinculin expression in cell peripheral region in addition to the nucleus area. Many FA spots around the cell boundary on Fn-Tigra are likely to be linked to actively developing filopodia of preosteoblasts, as identified via SEM observation (figure 3(*f*)).

3.5. Biophysical and biomechanical cell signals

In an attempt to correlate data obtained from various viewpoints (i.e. biological, biophysical and biomechanical), we utilized AFM to gain mechanistic information of differentiating preosteoblasts, in addition to biophysical changes, such as cell height (H), roughness, and cell spreading area (SA). Particular interest is the potential use of those biophysical

and biomechanical (*E*) factors as a means to determining the degree of cell differentiation. Cells are analyzed for their morphology and topography ($100 \times 100\,\mu\text{m}^2$) on days 1, 3, 7 and 14 via AFM (figure 7), and these results were subsequently quantified (figure 8). The average height of cells cultured on Fn-Tigra at day 1 was $2 \pm 0.06\,\mu\text{m}$ and increased with time by approximately 50% on day 14 (figures 7(*c*), (*f*), (*i*), (*l*) and 8(*a*)). A similar pattern was observed with cells cultured on Ti and Tigra. Cell morphology in figure 4 was found to be more widespread for cells cultured on Fn-Tigra than for those cultured on Ti and Tigra. Interestingly, the SA significantly declined from day 1 to 14, ranging from $1776\,\mu\text{m}^2$ to $299\,\mu\text{m}^2$ respectively, for cells cultured on Fn-Tigra (figure 8(*b*)). In comparison, cells cultured on the other groups exhibited a
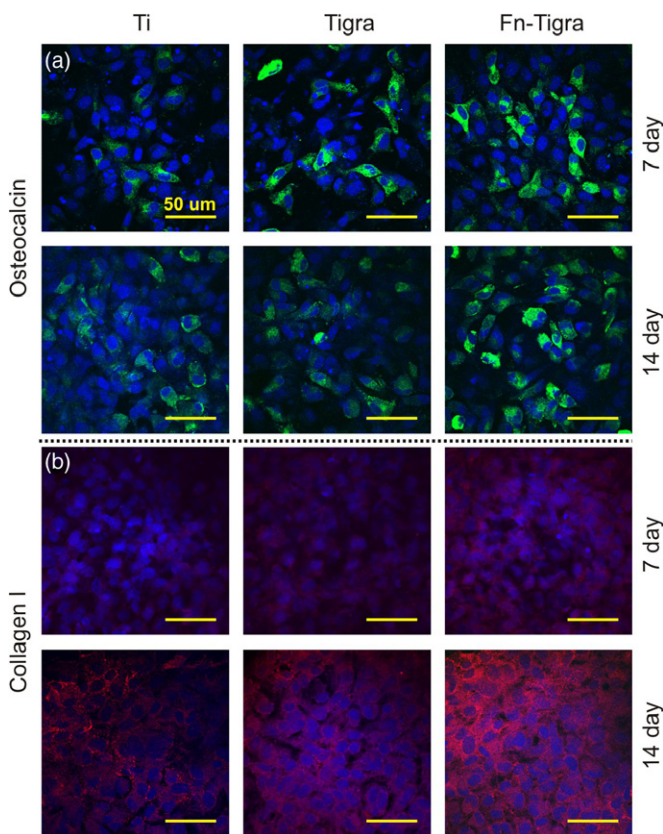
Figure 5. Investigation of osteogenic marker proteins produced by differentiating cells at days 7 and 14, respectively. The immunofluorescence images of preosteoblasts cultured on Ti, Tigra and Fn-Tigra show (*a*) OC (green) and (*b*) Col I (red). The nucleus is stained with DAPI (blue).

moderate decline of SA. This phenomenon can be explained by the increased number of cells with time in the given substrate area. The cell spreading area is inversely proportional to the cell height. Meanwhile, on day 1, the roughness of preosteoblasts cultured on Ti was higher than that of cells cultured on Fn-Tigra. This trend was reversed, however, on day 14, as the roughness of preosteoblasts was higher on Fn-Tigra than that of cells cultured on Ti; the roughness of cell surface on Fn-Tigra climbed from 575 nm to 777 nm during the given time period (figure 8(*c*)). It is closely related to the deposition of mineralized matrix with time. Furthermore, nanoindentation analysis was carried out on specific regions of cell surface (figures 7 and 8(*d*)). The average E for undifferentiated preosteoblasts was similar for each group on day 1; the E for cells on Ti, Tigra and Fn-Tigra was 2.8 ± 0.06, 2.8 ± 0.1 and 2.9 ± 0.1 KPa ($n = 3$, each group), respectively at different time points. During osteogenic differentiation, however, the cell stiffness increased considerably, up by 30% on day 14; the cell stiffness for cells cultured on Ti, on the other hand, showed only a 10% increase (figure 8(*d*)). Specifically, the stiffness of preosteoblasts on Fn-Tigra increased with time as follows: 2.9 ± 0.1 KPa (day 1), 3.09 ± 0.2 KPa (day 3), 3.39 ± 0.1 KPa (day 7) and 3.7 ± 0.1 KPa (day 14). These biomechanical results indicate that osteogenic cell differentiation accompanies a significant increase in the stiffness of preosteoblasts in a time-dependent manner, which coincide well with the current biological and biochemical assay-based data. Combining various analytical tools (biological, biochemical, biomechanical) in regard to cell adhesion and differentiation could further enrich our knowledge and play a crucial role in novel findings.
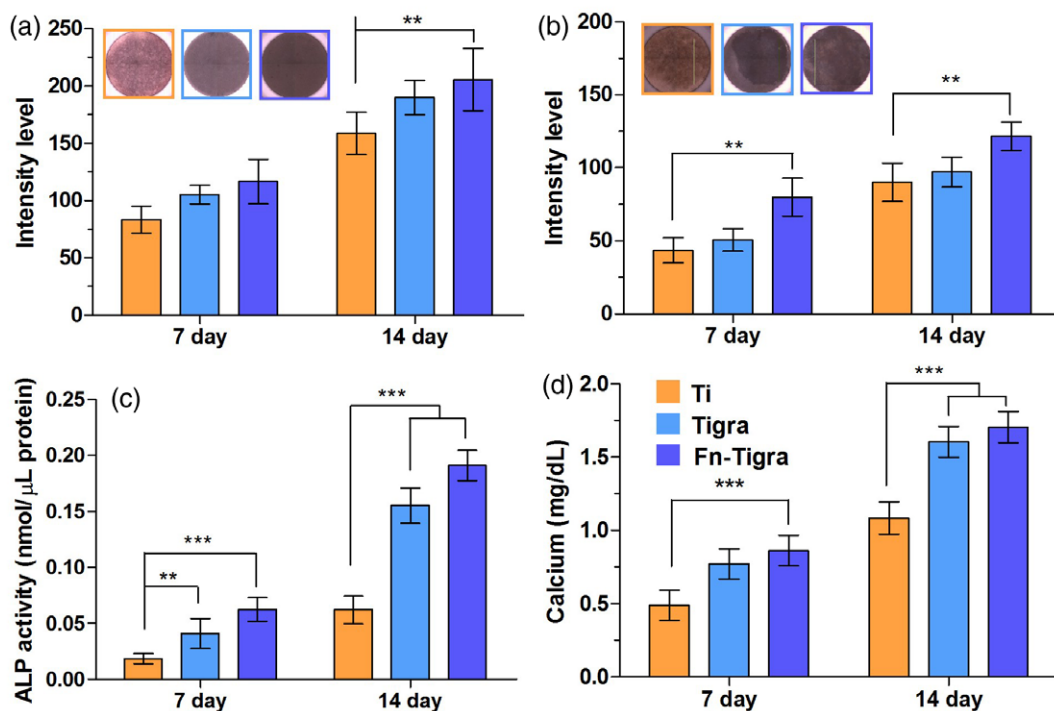

Figure 6. Quantitative results of osteogenic differentiation of preosteoblasts; (*a*) Alizarin red S, (*b*) von Kossa staining, (*c*) ALP activity and (*d*) calcium content at days 7 and 14, respectively. Cells cultured on Fn-Tigra exhibit an elevated calcium deposition and ALP activity when compared to those cultured on bare Ti. Statistically significant differences among Ti, Tigra, and Fn-Tigra are marked as * ($p < 0.05$), ** ($p < 0.01$) or *** ($p < 0.001$).
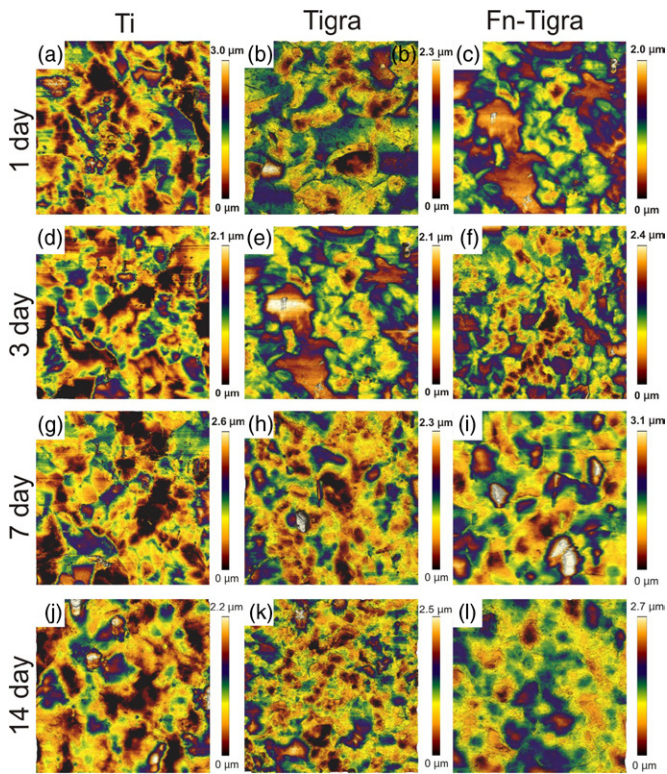
Figure 7. Observation of AFM scanning images of preosteoblasts differentiating with time *in vitro*. Images (100 × 100 μm² scale) were taken in a liquid contact mode on day 1 (*a*), (*b*), (*c*), day 3 (*d*), (*e*), (*f*), day 7 (*g*), (*h*), (*i*) and day 14 (*j*), (*k*), (*l*). The obtained data were processed using JPK software.

4. Conclusions

Development of physically or mechanically tunable micro-environments is of great importance in tissue engineering and stem cell study. In this work, fabrication of a GO-based artificial matrix in the form of Tigra and Fn-Tigra was successful. Fn-Tigra presented a unique surface texture with defined boundaries, significantly different from that of Ti. Upon investigation of Fn-Tigra with preosteoblasts, we found that the cell viability and proliferation were highest when cultured on Fn-Tigra compared to Ti and Tigra. In addition, the FA formation of cells on Fn-Tigra was clearly distinguished from those on Ti and Tigra. Furthermore, qualitative and quantitative examination of osteogenic differentiation on the various substrates demonstrated that Fn-Tigra provided a more osteogenic microenvironment than that provided by either Ti or Tigra. Biophysical properties, such as cell height and roughness, increased with culture time and were likely due partly to the deposition of mineralized matrix. Finally, an examination of cellular stiffness (E), a biomechanical factor, indicated a gradual increase over time for cells cultured on both Tigra and Fn-Tigra, whereas little change was observed for those cultured on Ti. Further investigations are warranted to fully understand whether standard biological markers correlate with biophysical or biomechanical ones. It is also notable that current experimental design with a rather short-term period may limit the validity of Fn-Tigra so that further work should include a long-term study. In summary, we demonstrate the feasibility of Tigra
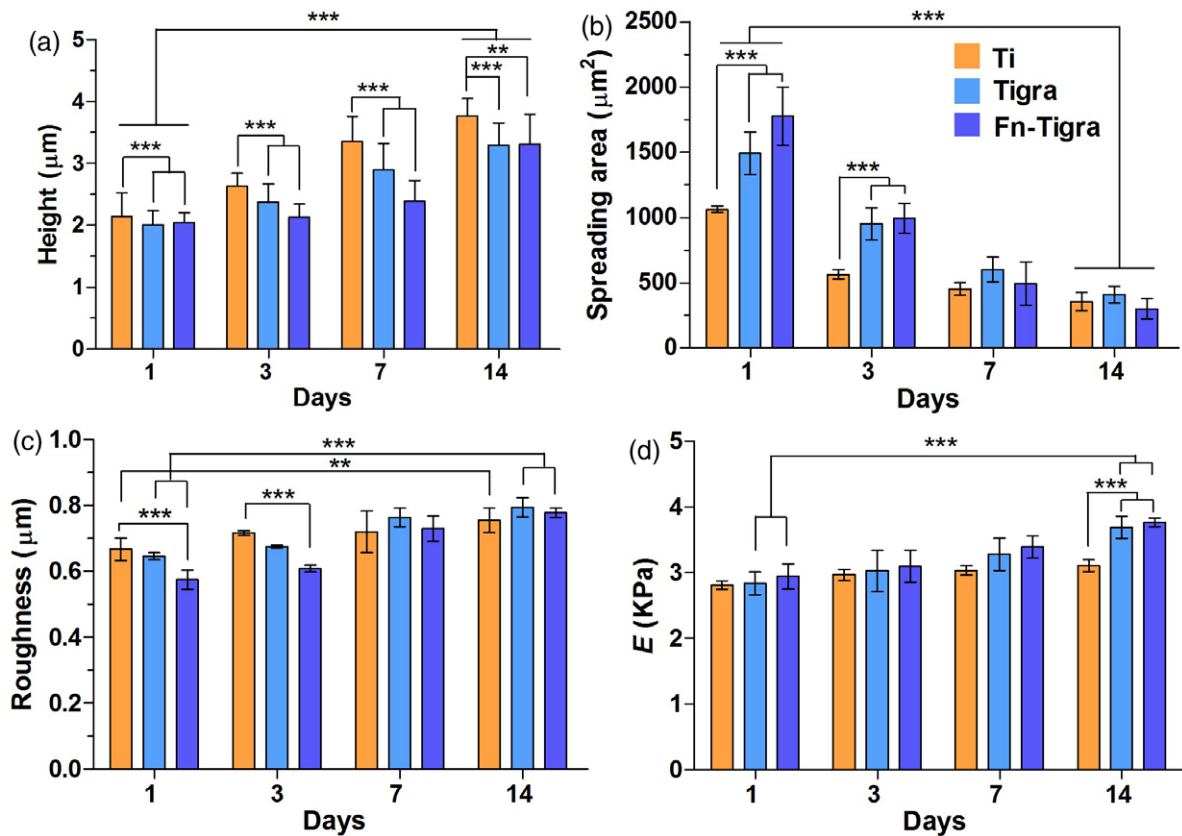

Figure 8. Quantitative analysis of biophysical and biomechanical parameters of preosteoblasts; (*a*) average cell height, (*b*) cell spreading area, (*c*) surface roughness, and (*d*) cell stiffness, Young's modulus (*E*). Statistically significant differences among Ti, Tigra, and Fn-Tigra are marked as ** ($p < 0.01$) or *** ($p < 0.001$).

artificial matrices as a tunable microenvironment platform for the immobilization of Fn, its potential use for bone tissue engineering applications and the use of *E* as an alternative of osteogenic biomarker.

Acknowledgments

References

[1] Chaudhuri O and Mooney D 2012 Stem-cell differentiation: anchoring cell-fate cues. *Nat. Mater.* **11** 568–9

[2] Kirmse R, Otto H and Ludwig T 2011 Interdependency of cell adhesion, force generation and extracellular proteolysis in matrix remodeling *J. Cell Sci.* **124** 1857–66

[3] Sadr N, Pippenger B E, Scherberich A, Wendt D, Mantero S, Martin I and Papadimitropoulos A 2012 Enhancing the biological performance of synthetic polymeric materials by decoration with engineered, decellularized extracellular matrix *Biomaterials* **33** 5085–93

[4] Lutolf MP and Hubbell JA 2005 Synthetic biomaterials as instructive extracellular microenvironments for morphogenesis in tissue engineering *Nat. Biotechnol.* **23** 47–55

[5] Lim H L, Chuang J C, Tran T, Aung A, Arya G and Varghese S 2011 Dynamic electromechanical hydrogel matrices for stem cell culture *Adv. Funct. Mater.* **21** 55–63

[6] Aravamudhan A, Ramos D M, Nip J, Harmon M D, James R, Deng M, Laurencin CT, Yu X and Kumbar SG 2013 Cellulose and collagen derived micro-nano structured scaffolds for bone tissue engineering *J. Biomed. Nanotechnol.* **9** 719–31

[7] Murugan R and Ramakrishna S 2006 Nano-featured scaffolds for tissue engineering: A review of spinning methodologies *Tissue Eng.* **12** 435–47

[8] Cipriano A F, De Howitt N, Gott S C, Miller C, Rao M P and Liu H 2014 Bone marrow stromal cell adhesion and morphology on micro- and sub-micropatterned titanium *J. Biomed. Nanotechnol.* **10** 660–8

[9] Kim B S, Park I K, Hoshiba T, Jiang H L, Choi Y J, Akaike T and Cho C S 2011 Design of artificial extracellular matrices for tissue engineering *Prog. Polym. Sci. (Oxford)* **36** 238–68

[10] Nardecchia S, Serrano M C, Gutiérrez M C, Portolés M T, Ferrer M L and Del Monte F 2012 Osteoconductive performance of carbon nanotube scaffolds homogeneously mineralized by flow-through electrodeposition. *Adv. Funct. Mater.* **22** 4411–20

[11] Yi C, Liu D, Fong C-C, Zhang J and Yang M 2010 Gold nanoparticles promote osteogenic differentiation of mesenchymal stem cells through p38 MAPK pathway *ACS Nano* **4** 6439–48

[12] Nayak T R, Andersen H, Makam V S, Khaw C, Bae S, Xu X, Ee P-LR, Ahn J-H, Hong BH, Pastorin G and Özyilmaz B 2011 Graphene for controlled and accelerated osteogenic differentiation of human mesenchymal stem cells *ACS Nano* **5** 4670–8

[13] Lee W C, Lim C H Y X, Shi H, Tang L A L, Wang Y, Lim C T and Loh K P 2011 Origin of enhanced stem cell growth and differentiation on graphene and graphene oxide *ACS Nano* **5** 7334–41

[14] Park S Y, Park J, Sim S H, Sung M G, Kim K S, Hong B H and Hong S 2011 Enhanced differentiation of human neural stem cells into neurons on graphene *Adv. Mater.* **23** H263–7

[15] Choi D H, Subbiah R, Kim I H, Han D K and Park K 2013 Dual growth factor delivery using biocompatible core–shell microcapsules for angiogenesis *Small* **9** 3468–76

[16] MacDonald D E, Markovic B, Allen M, Somasundaran P and Boskey A L 1998 Surface analysis of human plasma fibronectin adsorbed to commercially pure titanium materials *J. Biomed. Mater. Res.* **41** 120–30

[17] Dolatshahi-Pirouz A, Jensen T, Kraft D C, Foss M, Kingshott P, Hansen J L, Larsen A N, Chevallier J and Besenbacher F 2010 Fibronectin adsorption, cell adhesion, and proliferation on nanostructured tantalum surfaces *ACS Nano* **4** 2874–82

[18] Dolatshahi-Pirouz A, Jensen THL, Kolind K, Bünger C, Kassem M, Foss M and Besenbacher F 2011 Cell shape and spreading of stromal (mesenchymal) stem cells cultured on fibronectin coated gold and hydroxyapatite surfaces *Colloids Surf. B* **84** 18–25

[19] Li Q-L, Huang N, Chen J, Wan G, Zhao A, Chen J, Wang J, Yang P and Leng Y 2009 Anticoagulant surface modification of titanium via layer-by-layer assembly of collagen and sulfated chitosan multilayers *J. Biomed. Mater. Res. A* **89** 575–84

[20] Min S-K, Kang H K, Jang D H, Jung S Y, Kim O B, Min B-M and Yeo I-S Titanium surface coating with a laminin-derived functional peptide promotes bone cell adhesion *BioMed. Res. Int.* **8** 638348

[21] Keselowsky B G, Collard D M and Garcia A J 2003 Surface chemistry modulates fibronectin conformation and directs integrin binding and specificity to control cell adhesion *J. Biomed. Mater. A* **66** 247–59

[22] Subbiah R, Ramasundaram S, Du P, Hyojin K, Sung D, Park K, Lee N-E, Yun K and Choi K J 2013 Evaluation of cytotoxicity, biophysics and biomechanics of cells treated with functionalized hybrid nanomaterials *J. R. Soc. Interface* **10** 20130694

[23] Chaudhuri O, Parekh S H, Lam W A and Fletcher D A 2009 Combined atomic force microscopy and side-view optical imaging for mechanical studies of cells *Nat. Methods* **6** 383–7

[24] Plodinec M *et al* 2012 The nanomechanical signature of breast cancer *Nat. Nanotechnol.* **7** 757–65

[25] Henrich P B, Monnier C A, Halfter W, Haritoglou C, Strauss R W, Lim R Y H and Loparic M 2012 Nanoscale topographic and biomechanical studies of the human internal limiting membrane *Invest. Ophthalmol. Vis. Sci.* **53** 2561–70

[26] Stolz M *et al* 2009 Early detection of aging cartilage and osteoarthritis in mice and patient samples using atomic force microscopy *Nature Nanotechnol.* **4** 186–92

[27] González-Cruz R D, Fonseca V C and Darling E M 2012 Cellular mechanical properties reflect the differentiation potential of adipose-derived mesenchymal stem cells *Proc. Natl Acad. Sci. USA* **109** E1523–9

[28] Hummers W S and Offeman R E 1958 Preparation of graphitic oxide *J. Am. Chem. Soc.* **80** 1339–9

[29] Marcano D C, Kosynkin D V, Berlin D V J M, Sinitskii A, Sun Z, Slesarev A, Alemany L B, Lu W and Tour J M 2010 Improved synthesis of graphene oxide *ACS Nano* **4** 4806–14

[30] Yoshitomo H, Xianting D, Federico M, Akira W, Chih-ming H and Ichiro N 2013 Guiding the osteogenic fate of mouse and human mesenchymal stem cells through feedback system control *Sci. Rep.* **3** 1– 9

[31] Dolatshahi-Pirouz A, Jensen T, Foss M, Chevallier J and Besenbacher F 2009 Enhanced surface activation of

fibronectin upon adsorption on hydroxyapatite *Langmuir* **25** 2971–8

[32] Rabe M D, Verdes D and Seeger S 2011 Understanding protein adsorption phenomena at solid surfaces *Adv. Colloid Interface Sci.* **162** 87–106

[33] Huh S H 2011 Thermal reduction of graphene oxide *Thermal Reduction of Graphene Oxide, Physics and Applications of Graphene—Experiments* ed S Mikhailov 73–90

[34] Wilson C J, Clegg R E, Leavesley D I and Pearcy M J 2005 Mediation of biomaterial–cell interactions by adsorbed proteins: a review *Tissue Eng.* **11** 1–18

[35] Teo B K, Wong S T, Lim C K, Kung T Y, Yap C H, Ramagopal Y, Romer L H and Yim E K 2013 Nanotopography modulates mechanotransduction of stem cells and induces differentiation through focal adhesion kinase *ACS Nano* **7** 4785–98